Paper B

Waves generated by a pressure disturbance moving in a channel with a variable cross section topography.

*

* To be submitted.

Waves generated by a pressure disturbance moving in a channel with a variable cross section topography

Tomas Torsvik, Geir Pedersen, Kristian Dysthe

Date of printing: December 13, 2006

Abstract

The present work is a numerical investigation on waves generated by a pressure disturbance moving at constant speed in a channel with a variable cross-channel depth profile. The channel profile, which is uniform in the along-channel direction, has a deep trench located in the vicinity of the center line of the channel, and shallow banks near the channel walls. Wave fields generated upstream and downstream of the moving pressure disturbance are described, and the characteristic features present in the wave patterns are related to the parameters governing the speed of the pressure disturbance and the shape of the cross-channel profile. Our numerical investigation is based on the COULWAVE long wave model, which solves a set of Boussinesq type equations in two horizontal dimensions.

1 Introduction

In coastal waters, ships are often required to navigate in natural or dredged trenches. Long waves are known to be generated by high speed vessels traveling at speeds close to the critical depth Froude number $F = U/\sqrt{gh}$, where U is the speed of the vessel, g is the acceleration of gravity and h is the depth. In order to examine how ship waves behave under these conditions, we consider the idealized case where waves, generated by a moving pressure disturbance, propagate in a channel with a deep trench at the centre line and shallow banks along the channel walls. We are particularily interested in cases where the speed of the pressure disturbance is subcritical with respect to the Froude number in the trench, but near critical or supercritical with respect to the shallow banks. Because the ship wave pattern changes substantially in the transition between the subcritical and supercritical regime, these test may provide us with a better understanding on how the different features in the bathymetry influences the wave pattern.

Several researchers have studied waves propagating in channels with arbitrary cross-section profiles[15, 14] and the wave patterns, in two horizontal dimensions (2HD), generated by a disturbance moving at speeds close to the critical Froude number in channels with a rectangular cross-section profile[1, 3, 13]. Mathew and Akylas[10] brought these elements together in their study of waves propagating in channels with a trapezoidal cross-section profile. Recently, Teng and Wu[19], Jiang et al.[2], and Liu and Wu[5] have made contributions to this field of research. Most of these studies deal with channels with trapezoidal cross-section profiles, but Jiang et al.[2] also include results for a channel with a deep trench along the center line, which is similar to the cases that will be discussed in this paper.

In our study, we simulate the wave generation and propagation using COULWAVE, a computer model for long waves, developed at Cornell University by Lynett, Wu and Liu[7, 8, 6]. The model is based on a set of weakly dispersive, fully nonlinear Boussinesq equations, first developed by Liu[4] and Wei et al.[20]. The horizontal velocity components are evaluated at a reference depth $z_\alpha = 0.531h$, resulting in an improvement of the dispersive properties of the equations relative to the standard depth integrated formulation, as shown by Nwogu[12]. A version of the model which includes a pressure disturbance has been implemented by Liu and Wu[5].

2 Mathematical model equations

The numerical model is based on a set of fully nonlinear and weakly dispersive Boussinesq equations, which are nondimensionalized by introducing the characteristic depth h_0, as the length scale, $\sqrt{g/h_0}$ as the time scale, and the hydrostatic pressure $\rho g h_0$, as the pressure scale. In dimensionless form, the Boussinesq equations consist of the continuity equation

$$\begin{aligned}
&\frac{\partial \zeta}{\partial t} + \nabla \cdot [(\zeta + h)\mathbf{u}_\alpha] \\
&\quad + \nabla \cdot \left\{ \left(\frac{z_\alpha^2}{2} - \frac{h^2}{6} \right) h \nabla (\nabla \cdot \mathbf{u}_\alpha) + \left(z_\alpha + \frac{h}{2} \right) h \nabla [\nabla \cdot (h\mathbf{u}_\alpha)] \right\} \\
&\quad + \nabla \cdot \left\{ \zeta \left[\left(z_\alpha - \frac{1}{2}\zeta \right) \nabla (\nabla \cdot (h\mathbf{u}_\alpha)) + \frac{1}{2} \left(z_\alpha^2 - \frac{1}{3}\zeta^2 \right) \nabla (\nabla \cdot \mathbf{u}_\alpha) \right] \right\} \\
&\quad = 0\,,
\end{aligned} \tag{1}$$

and the momentum equation

$$
\begin{aligned}
&\frac{\partial \mathbf{u}_\alpha}{\partial t} + (\mathbf{u}_\alpha \cdot \nabla)\mathbf{u}_\alpha + \nabla\zeta + \nabla p \\
&\quad + \left\{ \nabla \left[z_\alpha \left(\nabla \cdot \left(h \frac{\partial \mathbf{u}_\alpha}{\partial t} \right) \right) \right] + \nabla \left[\frac{1}{2} z_\alpha^2 \left(\nabla \cdot \frac{\partial \mathbf{u}_\alpha}{\partial t} \right) \right] \right\} \\
&\quad + \nabla \left\{ \frac{1}{2} z_\alpha^2 \mathbf{u}_\alpha \cdot \nabla(\nabla \cdot \mathbf{u}_\alpha) + z_\alpha \mathbf{u}_\alpha \cdot \nabla(\nabla \cdot h\mathbf{u}_\alpha) \right. \\
&\quad \left. + \frac{1}{2}[\nabla \cdot (h\mathbf{u}_\alpha)]^2 - \zeta \nabla \cdot \left(h \frac{\partial \mathbf{u}_\alpha}{\partial t} \right) \right\} \\
&\quad + \nabla \left\{ \zeta(\nabla \cdot h\mathbf{u}_\alpha)(\nabla \cdot \mathbf{u}_\alpha) - \frac{1}{2}\zeta^2 \nabla \cdot \left(\frac{\partial \mathbf{u}_\alpha}{\partial t} \right) - \zeta \mathbf{u}_\alpha \cdot \nabla(\nabla \cdot h\mathbf{u}_\alpha) \right\} \\
&\quad + \nabla \left\{ \frac{1}{2}\zeta^2 (\nabla \cdot \mathbf{u}_\alpha)^2 - \frac{1}{2}\zeta^2 \mathbf{u}_\alpha \cdot \nabla(\nabla \cdot \mathbf{u}_\alpha) \right\} = 0\,,
\end{aligned} \tag{2}
$$

where $\zeta(x, y, t)$ is the surface displacement, $\mathbf{u}_\alpha(x, y, t) = (u_\alpha(x, y, t), v_\alpha(x, y, t))$ is the velocity at the depth $z = z_\alpha$, $\nabla = (\partial/\partial x, \partial/\partial y)$ is the horizontal gradient operator, ρ is the density of water and $p(x, y, t)$ is the pressure disturbance of magnitude p_a at the free surface. The reference depth $z_\alpha = -0.531h$ is applied, following the recommendation by Nwogu[12]. This optimizes the dispersive properties of the equations by matching the Padé[2,2] approximation of the linear dispersion relation of Stokes. With the model equations formulated as above, wave propagation in terms of phase velocity and group velocity is accurately described for waves with dimensionless wave number in the range $0 < kh \leq \pi$, as shown by Madsen and Schäffer[9].

When deriving (1) and (2), it is assumed that the characteristic water depth h_0, is small relative to the horizontal length scale λ, i.e. $\mu = h_0/\lambda \ll 1$. The characteristic wave amplitude a may be of the same order of magnitude as h_0, and the nonlinear effects, related to the parameter $\epsilon = a/h_0 = O(1)$ are not required to be weak. The model equations (1) and (2) are accurate up to $O(\mu^2)$.

Numerical method

The COULWAVE model applies an algorithm which is similar to the method of Wei et al.[20]. The algorithm is formally accurate to Δt^4 in time. The first-order spatial derivatives in the equations are discretized to fourth order, whereas the spatial derivatives in the dispersive terms are discretized to second order. This ensures that the numerical dispersion related to the spatial derivatives of first order is of higher order than the physical dispersive terms. The algorithm is marched forward in time using the Adams-Bashforth-Moulton predictor-corrector scheme to update the dependent variables.

Although the algorithm is formally of second order in space, this convergence rate has not been achieved in the simulations. The numerical results converge when the grid resolution is increased, but the convergence is slow for the steep, large amplitude waves often found immediately downstream of the pressure disturbance. A five point filter has been applied to avoid saw-tooth noise which tends to emerge in the cross-channel direction. A small damping is also inherent in the time stepping scheme. No other dissipative terms have been added to smooth the variable fields. The model has been tested by running the same simulation with spatial grid resolutions of $0.1\,h_0$, $0.2\,h_0$, and $0.4\,h_0$. Using the finest resolution as reference, we calculated the relative errors E_u and E_d, for the amplitudes of the leading upstream wave and the first downstream wave, respectively. For $\Delta x = \Delta y = 0.4\,h_0$, the errors $E_u = 2.0 \cdot 10^{-2}$ and $E_d = 2.5 \cdot 10^{-1}$ were found, while increasing the grid resolution to $\Delta x = \Delta y = 0.2\,h_0$, reduced the errors to $E_u = 4.5 \cdot 10^{-3}$ and $E_d = 7.1 \cdot 10^{-2}$. A spatial grid resolution of $\Delta x = \Delta y = 0.2\,h_0$ has been used for all subsequent simulations in this paper.

The pressure disturbance is often required to travel a length of order $O(10^3 h_0)$ for the wave pattern to fully develop. In order to speed up the computation, the wave field is only computed in a window including the parts of the channel immediately upstream and downstream of the pressure disturbance. This window is shifted upstream when the free surface displacement grows to $\delta = 0.05\,p_a$ somewhere along a cross-channel line located $30\,h_0$ downstream of the upstream boundary. A potential problem with this method is contamination from waves generated at the downstream boundary, which is of particular concern for simulations where the Froude number is subcritical. By running the same simulation with different sizes of computational windows, we found that by the end of the simulation, the error was $O(10^{-8})$ at $50\,h_0$ downstream of the pressure disturbance, and $O(10^{-3})$ near the downstream boundary of the smallest computational window, located $88.5\,h_0$ downstream of the pressure disturbance. We also tested for the sensitivity to the shifting criteria by running the model with $\delta = 0.01\,p_a$. The errors were found to be $O(10^{-5})$ everywhere, except near the downstream boundary.

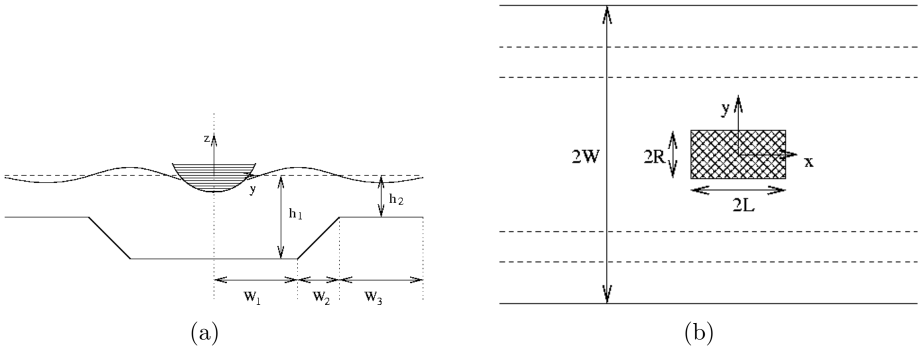

Figure 1: Channel cross-sectional profile

3 Results

In this section we present results based on numerical simulations where waves are generated by a moving pressure disturbance in a channel with a variable cross-channel topography. The channel has a deep section along the center line and shallow banks near the solid boundaries. The parameters for the cross-channel variation are defined according to Fig. 1. This cross-channel profile is similar to one of the examples discussed by Jiang et al.[2]. A direct comparison between our results and the result presented in Jiang et al.[2] has not been attempted, because Jiang et al. does not quantify the free surface displacement attained in their simulation. Results will generally be shown for the half plane $0 \leq y \leq W$ only, since the wave pattern will be symmetrical across the line $y = 0$.

The forcing pressure disturbance is defined according to

$$p(x + Ft, y) = p_a f(x + Ft) q(y)\,,$$

$$f(x + Ft) = \cos^2\left[\frac{\pi(x + Ft)}{2L}\right]\,, \quad -L \leq x + Ft \leq L\,,$$

$$q(y) = \cos^2\left(\frac{\pi y}{2R}\right)\,, \quad -R \leq y \leq R\,,$$

on $-L \leq x + Ft \leq L$, $-R \leq y \leq R$, and is zero outside this rectangle. Typical values for the pressure disturbance is $p_a = 0.1$, $L = 4.0h_0$, and $R = 2.0h_0$. In the following figures, the pressure disturbance moves towards decreasing values of x, and the along-channel coordinate is redefined as

$$\xi = x + Ft\,,$$

in which the location of the pressure disturbance remains fixed at all times. In this frame of reference, upstream waves are located to the left of the pressure disturbance. At the start of the simulation, the pressure disturbance is abruptly set in motion at a particular speed, which is maintained constant thereafter.

3.1 Influence of the Froude number on the wave pattern

In this part we examine how the wave pattern is influenced by changing the velocity of the advancing pressure disturbance. The channel is defined by $W_1 = 3.0$, $W_2 = 2.0$, $W_3 = 5.0$, $h_1 = 1.0$ and $h_2 = 0.6$, and the velocities used in the simulations corresponds to Froude numbers at the trench of $F_1 = 0.7$, 0.8, 0.9 and 1.0, which give Froude numbers $F_2 = 0.9037$, 1.0328, 1.1619 and 1.2910, respectively, at the shallow banks. Figure 2 shows contour plots of the generated waves at $t = 1253$, figure 3 shows the leading downstream waves in greater detail, and figure 4 shows along-channel wave profiles at $y = 0$, 5 and 10.

For $F_1 = 0.7$ and $F_2 = 0.9037$, the upstream wave generation, shown if Figs. 2(a) and 4(a), seems to be transient in nature, and depends on the startup of the simulation (see discussion in section 3.5). In the region immediately upstream of the pressure disturbance, both the wave amplitude and the mean surface elevation tend to zero with time. A steady state is attained downstream of the pressure disturbance, shown in figure 3(a), where the wave pattern consists of small amplitude waves with wave lengths of $\lambda \approx 3$. Since $hk \approx 2$ is within the range where the wave dispersion is accurately described, we can expect the results to be reasonable even for these short waves. This is a case which clearly demonstrates the advantage of using Boussinesq models with improved dispersion properties instead of the standard form of the Boussinesq equations.

The leading part of the upstream wave in figure 4(a) resembles the Airy function $Ai(\xi)$, which is the traveling wave solution for the linearized equations. These waves display only a slight cross-channel variation in amplitude and no cross-channel variation in phase speed despite the significant cross-channel variation in depth. It may seem strange that an essentially linear waves should not be influenced by the depth variation. In this case the leading waves are long not only with respect to the depth, but also with respect to the width of the channel, and is therefore only influenced by the mean depth in the channel. This is also consistent with the fact that the cross-channel variation increases as the wave length decreases in the wave train.

When the Froude number is increased to $F_1 = 0.8$ and $F_2 = 1.0328$, an undular bore is generated upstream of the moving pressure disturbance, as

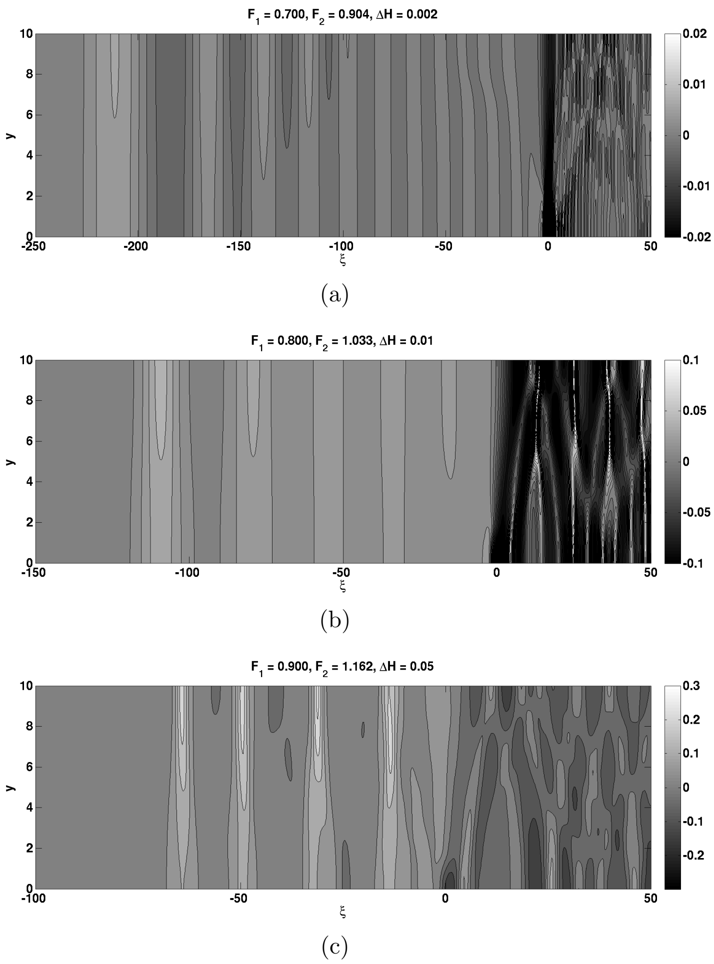

Figure 2: Contour plot of waves generated at different Froude numbers. Contour levels given by ΔH for each plot.

seen in Figs. 2(b) and 4(b). We note that the wave crests of the upstream waves span the channel at an angle which is nearly perpendicular to the channel wall, and that the amplitude, although higher at the wall than at the center of the channel, varies only slightly in the cross-channel direction. Waves with large amplitudes are generated downstream of the pressure field for $F_1 = 0.8$. These high amplitudes occur near the channel wall ($y = 10$) due to wave reflection at the solid boundary, but also in the shallow part of the channel ($5 < y < 8$) due to wave-wave interaction.

While the waves generated for $F_1 = 0.7$ and $F_1 = 0.8$ clearly conforms to

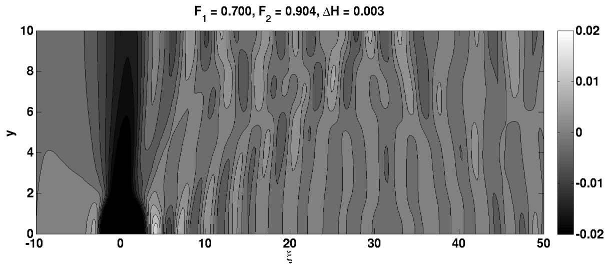

(a)

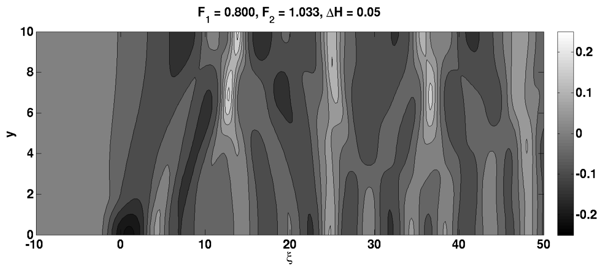

(b)

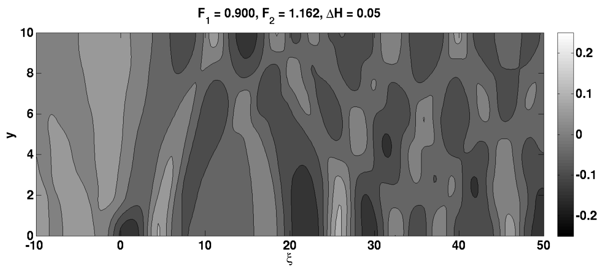

(c)

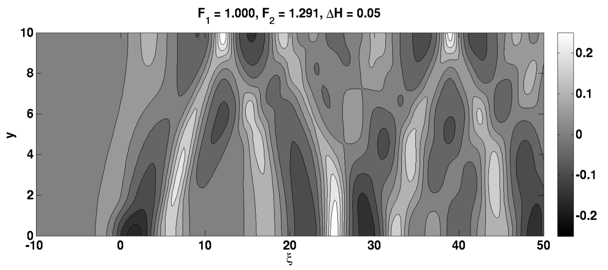

(d)

Figure 3: Details of the downstream wave pattern.

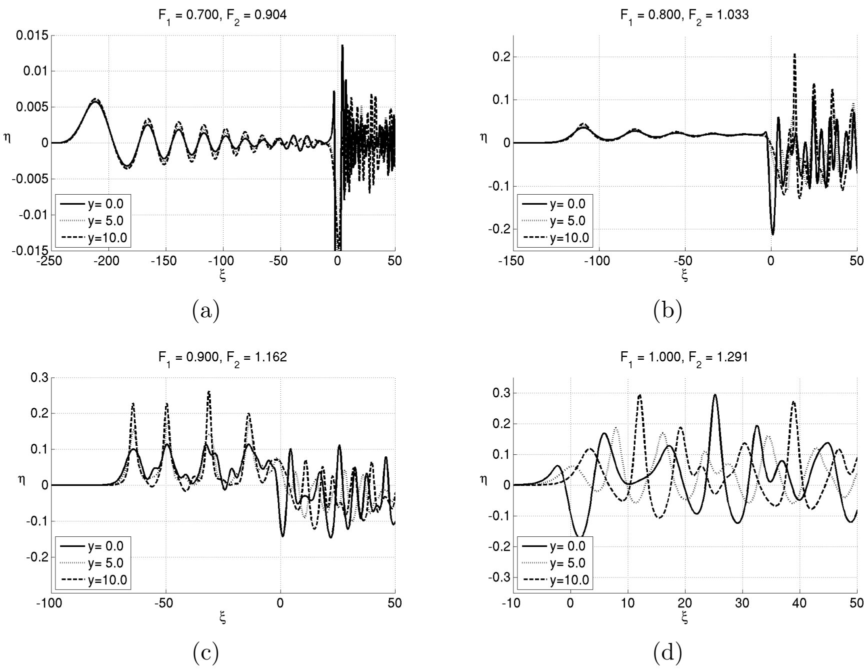

Figure 4: Wave cuts along the channel.

subcritical wave patterns, the wave pattern generated at $F_1 = 0.9$ and $F_2 = 1.1619$, seen in Figs. 2(c) and 4(c), shows what appears to be a persistent generation of upstream waves which is chracteristic for the near critical wave pattern. It is notable that this wave pattern occurs when the local Froude number at the trench is still subcritical. The leading upstream wave attains the bell-shaped form often associated with solitary waves, but is trailed by small amplitude disturbances which interact with the following upstream waves. A similar phenomenon was found by Mathew and Akylas[10] for an undular bore propagating in a trapezoidal channel. The wave diffraction due to depth variation is more prominent in the middle of the channel than at the channel walls, as seen in Fig. 4(c). Even though wave diffraction occurs, causing significant variation in amplitude and wave profiles in the cross-channel direction, each of the upstream waves can be clearly identified as distinct waves with wave crests oriented nearly perpendicular to the channel wall. The amplitudes of the downstream waves for $F_1 = 0.9$, seen in Fig. 3(c), are of the same order of magnitude as for $F_1 = 0.8$, and the largest peaks are located near the center line of the channel and near the channel walls.

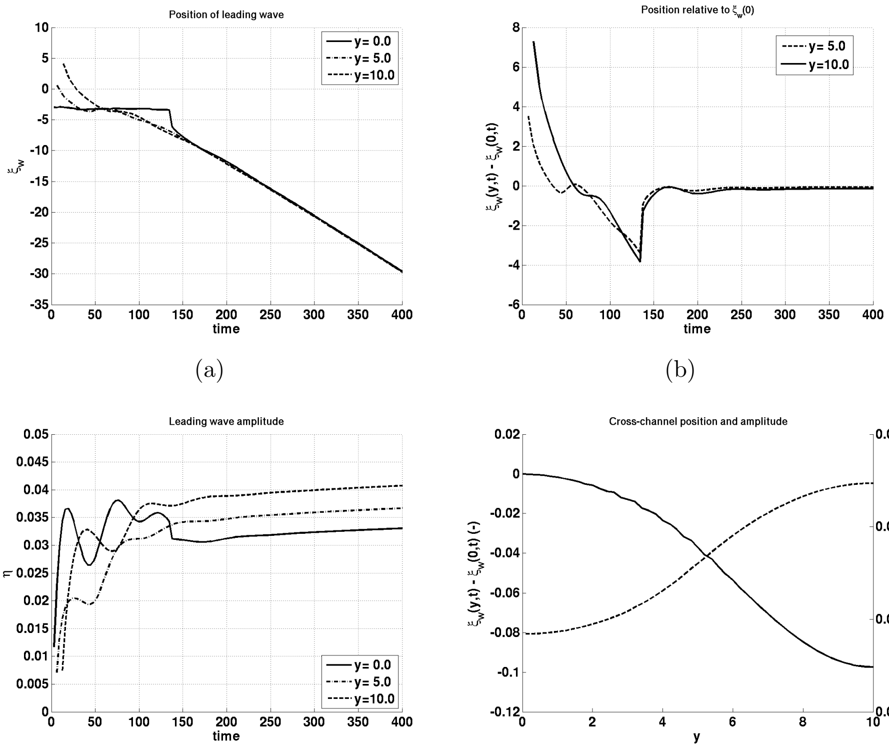

(a) (b) (c) (d)

Figure 5: Leading upstream wave. $F = 0.8$.

Waves do not propagate upstream of the pressure field for $F_1 = 1.0$ and $F_2 = 1.2910$, so the wave pattern consists only of the downstream waves, as seen in Figs. 3(d) and 4(d). The leading wave is reflected at the wall, but this does not cause the wave to propagate upstream. Large amplitude waves are found downstream of the pressure field. These waves are amplified near the solid boundary ($y = 10$) and the center line of the channel.

3.2 Waves radiated upstream of the pressure field

For $F_1 = 0.8$, the upstream waves propagate as an undular bore. The position of the leading wave crest $\xi_w(y, t)$ is plotted in figure 5(a), for $y = 0$, 5, and 10. Early in the simulation, the position of the leading wave is located further upstream at the center of the channel than at the channel walls. While the wave crest at the center line initially remains nearly stationary compared to the position of the pressure disturbance, with $\xi_w(0, t) = -3.3 \pm 0.1$, the wave

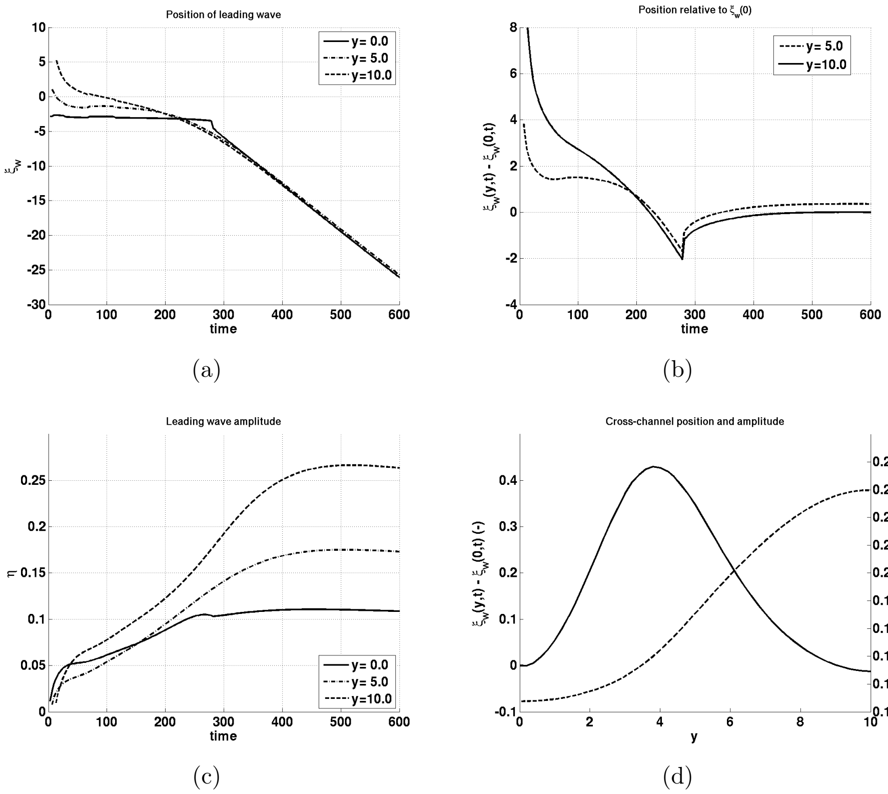

Figure 6: Leading upstream wave. $F = 0.9$.

crest at the channel wall is seen to propagate upstream. The straightening of the wave crest at the channel wall and the upstream propagation is clearly a feature of Mach reflection, which was previously found by Pedersen[13] to occur for waves generated in channels with a rectangular cross-channel profile.

The wave propagation at the wall slows down at $t \approx 75$, when the wave creast has become nearly a straight line, as seen in figure 5(b), where the position of the wave crest $\xi_w(y, t)$ is plotted relative to $\xi_w(0, t)$. This coincides with a temporary slump in the wave amplitude at the wall, as seen in figure 5(c). Once the wave amplitude at the wall increases, the waves crest over the shallow bank propagate a considerable distance upstream of the crest at the center line, before an abrupt adjustment occurs at $t \approx 135$, which brings the wave crest at the center line into alignment with the wave crest near the channel wall. From figure 5(a) it is apparent that the adjustment shifts the central part of the upstream wave forward to the position of the wave near the channel wall. After the adjustment, the leading wave propagate with a constant speed c_w of approximately $c_w/U = 1.12$, which is subcritical ($c_w/\sqrt{h_1} = 0.89$) at $y = 0$ and supercritical ($c_w/\sqrt{h_2} = 1.15$) at $y = 10$. The cross-channel amplitude increases from the center line to the channel wall, as shown by the stapled line in figure 5(d), and the mean wave amplitude is increasing slowly with time, as seen in figure 5(c). This may however be a transient phenomenon, because the upstream waves form an undular bore which is not fully developed within the time shown, which means that wave energy is still transfered to the leading wave from the rear. The wave crest is located slightly further upstream near the channel wall than the center line, as seen by the solid line in figure 5(d).

The generation of the leading upstream wave for $F_1 = 0.9$ follow much the same pattern as for $F_1 = 0.8$. At the start of the simulation, the upstream crest at $y = 0$ is stationary at $\xi_w(0, t) = -3.2 \pm 0.3$, but adjusts to the wave crest in the far field at $t \approx 280$, as seen in Fig. 6(a). The wave crest is located nearly the same distance upstream near the center line and near the channel wall, but lags behind by $0.4h_0$ at $y = 4$, as seen in figure 6(d). The wave amplitude decreases with time, as seen in figure 6(c), which is to be expected because the wave is subject to wave diffraction. The wave propagates at approximately $c_w/U = 1.07$, which is subcritical ($c_w/\sqrt{h_1} = 0.96$) at $y = 0$ and supercritical ($c_w/\sqrt{h_2} = 1.25$) at $y = 10$.

3.2.1 Comparison with cross-channel averaged theory

For the channel configurations used in the examples above, we often find that the leading upstream wave is long compared to the width of the channel. These results may therefor be comparable to results using cross-channel averaged models, which were first developed by Peters[15] and Peregrine[14], and have more recently been applied by Teng and Wu[17]. The models are based on weakly nonlinear and dispersive equations, such as KdV and standard Boussinesq equations, and are developed under the assumption that the cross-channel variation of the velocity and wave amplitude is small compared to the along-channel variation. Under these conditions, it is possible to determine the solitary wave solution analytically, given a mean wave amplitude and a specific cross-channel depth profile. The procedure is briefly outlined in the appendix.

Figure 7 shows a comparison between the leading upstream wave at $\zeta = \xi - \overline{\xi}_w$, found in the simulations with the COULWAVE model, and wave solutions from the Teng-Wu (TW) cross-channel averaged model. For $F_1 = 0.7$, it is appropriate to compare the simulated result in figure 7(a) with the Airy function, which is the solution in the linearized TW model. In the

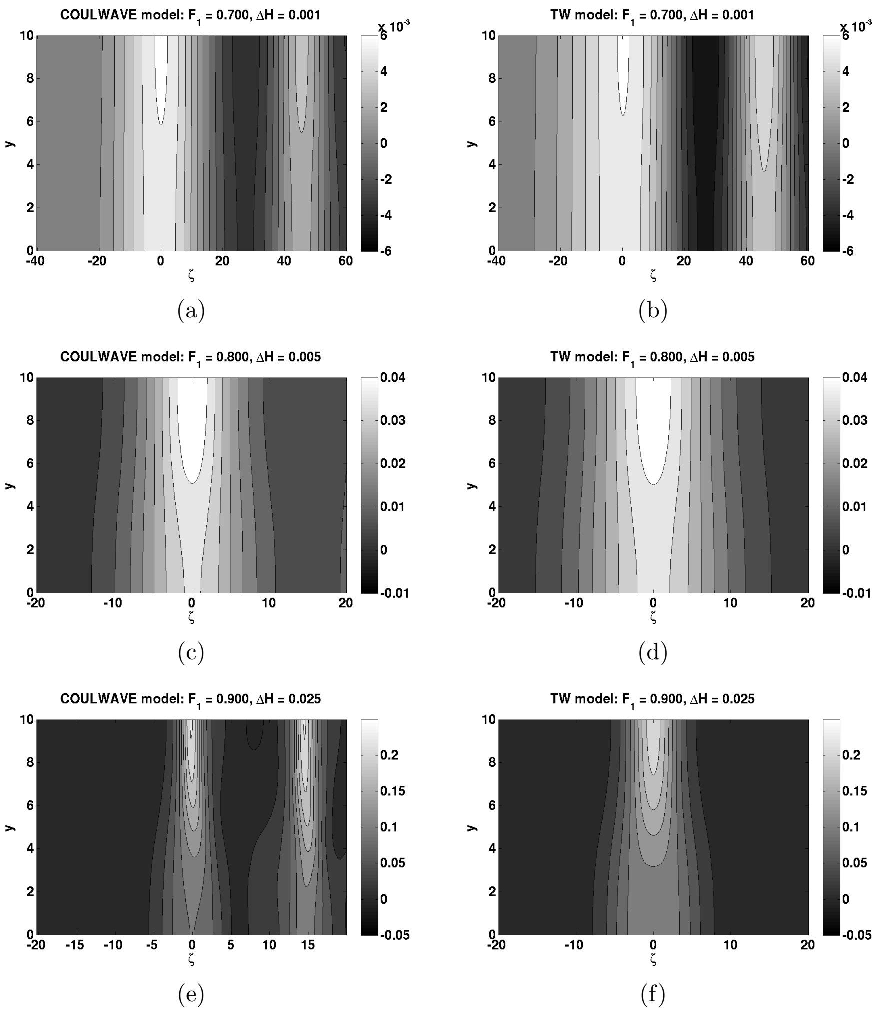

Figure 7: Comparison between TW and COULWAVE models.

simulated result, the leading wave has a steeper wave front and the trailing waves are smaller than for the TW model result based on the Airy function. This may be due to nonlinear effects, which are small but not negligible for these waves. There is however a good agreement between the models on the cross-channel amplitude variation, which deviates by approximately $\pm 1.2\%$ at the centre line and at the channel wall. The results for $F_1 = 0.8$ and $F_1 = 0.9$ are compared to the corresponding solitary wave solution of TW with the same mean amplitude. Results for $F_1 = 0.8$, shown in figures 7(c) and 7(d), are in reasonable agreement. The cross-channel variation in amplitude is smaller than for the COULWAVE model, resulting in a deviation between the amplitudes of approximately ±2.5% at the center line and at the channel wall. The wave crest of the TW solitary wave is also broader than the wave crest in the COULWAVE model. For $F_1 = 0.9$, the TW solitary wave solution is not in agreement with the COULWAVE result. The leading wave in the COULWAVE simulation has a wave length that is comparable with the channel width, and is therefor influenced by the cross-channel depth variation. Because of the short wave length, it may also be influenced by the waves following in the wave train. These results show that cross-channel averaged theory may be applicable for small amplitude solitary waves propagating in channels with a variable cross-section topography, but only if the wave length is large compared to the channel width.

Figure 7 shows the comparison between the solitary wave solution from the Teng-Wu (TW) cross-channel averaged model and the leading upstream wave at $\zeta = \xi - \overline{\xi}_w$, found in the simulations with the COULWAVE model. The best match is achieved for $F_1 = 0.8$, shown in figures 7(c) and 7(d). The cross-channel variation in amplitude is smaller than for the COULWAVE model, resulting in a deviation between the amplitudes of approximately ±2.5% at the center line and at the channel wall. The wave crest of the TW solitary wave is also broader than the wave crest in the COULWAVE model. For $F_1 = 0.7$, the amplitude deviation is approximately ±2.1% at the center line and channel wall, but now the wave length of the TW solitary wave is significantly longer than the leading wave in the COULWAVE model. This result is consistent with our previous assertion that the upstream wave behaves like an Airy function, and does not develop independent solitary waves. For $F_1 = 0.9$, the TW solitary wave solution is not in agreement with the COULWAVE result. The leading wave in the COULWAVE simulation has a wave length that is comparable with the channel width, and is therefor influenced by the cross-channel depth variation. Because of the short wave length, it may also be influenced by the waves following in the wave train. These results show that cross-channel averaged theory may be applicable for small amplitude solitary waves propagating in channels with a variable cross-section topography, but only if the wave length is large compared to the channel width.

3.3 Amplification in the wake wave pattern

Wave amplification due to wave-wave interaction can sometimes occur in the downstream wave pattern, as seen in figure 3(b). The strongest amplification is located at approximately $\xi = 10$ and $y = 7$, where the first reflected wave

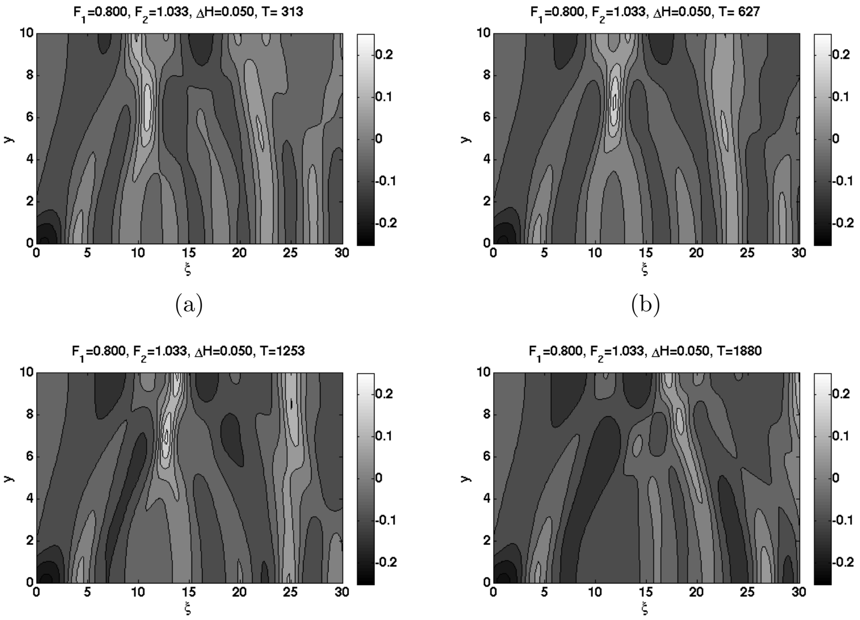

(a) (b) (c) (d)

Figure 8: Wave amplification due to wave-wave interaction

in the downstream wave packet interacts with the second downstream wave. A similar feature is present at approximately $\xi = 35$. A time sequence of the downstream wave pattern is shown in figure 8, and the temporal development of the amplitude of the leading downstream wave at $y = 7$ and the two leading waves at $y = 10$ is shown in figure 9. At first, the wave amplification grows with increasing amplitude of the reflected leading wave, as seen in figure 8(a). The amplitude of the leading wave peaks at approximately $t = 340$, attaining an amplitude of $\eta = 0.157$ at the channel wall, and steadily declines after this time. The amplitude of the wave at $y = 7$ continues to increase as the second downstream wave grows large. Due to the decreasing amplitude of the leading wave, the amplified wave at $y = 7$ can not be sustained indefinitely, and the amplitude decreases significantly after $t = 1500$.

Amplification due to wave-wave interaction has been found in test cases with a slightly different depth profile ($W_1 = 4$, $W_2 = 2$, and $W_3 = 4$), and with different velocity of the pressure disturbance ($F_1 = 0.9$, $W_1 = 6$, $W_2 = 2$, and $W_3 = 2$), as seen in figure 10. It is not clear at this point whether these amplified waves will always be transient, or if they can occur in the wave pattern after a steady state has been attained. Wave amplification due to wave-wave interaction has also been observed in channels with a rectangular

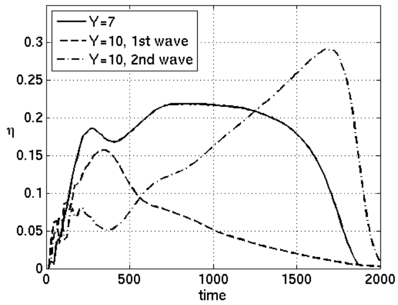

Figure 9: Time development of wave amplification

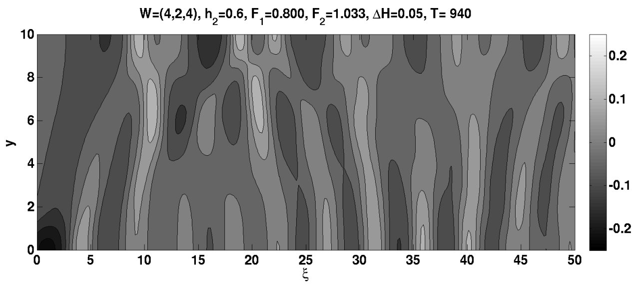

(a)

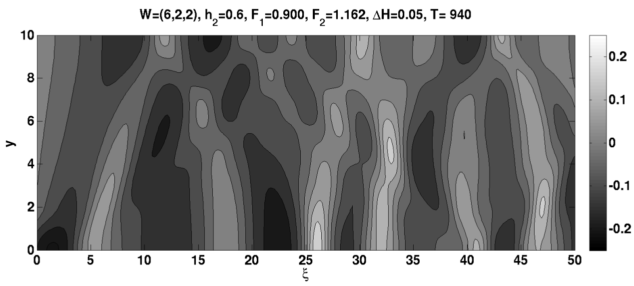

(b)

Figure 10: Wave amplification due to wave-wave interaction

cross-section profile, where the waves were generated by two pressure patches of equal size in a configuration resembling the hull of a catamaran, indicating that a cross-channel depth variation is not a necessary condition for this phenomenon. A similar phenomenon has been discussed by Peterson et al.[16], who studied extreme waves occuring in the intersection of two solitary wave groups. In that paper, it is suggested that such a phenomenon may occur

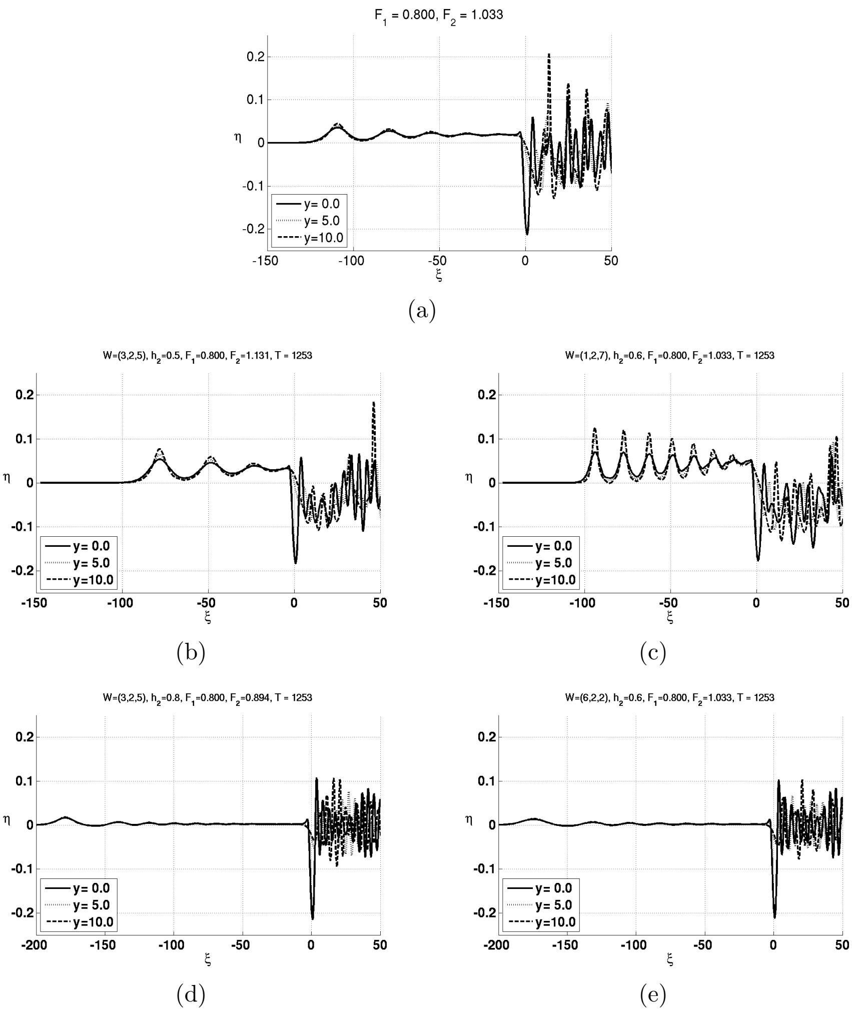

Figure 11: Wave cuts along the channel.

when two high speed vessels meet, or as a result of navigation.

3.4 Results for different channel parameters

We now consider how changes in the channel width parameters $W = (W_1, W_2, W_3)$, and channel depth parameter h_2 (keeping $h_1 = 1$), influences the wave pattern. In this section the Froude number at the trench is maintained at $F_1 = 0.8$. Figure 11 show wave cuts along the channel for five test cases. Figure 11(a) corresponds to the case described earlier, with $W = (3, 2, 5)$,

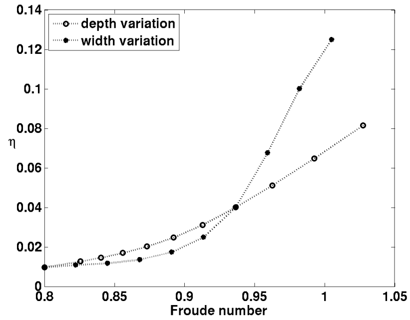

Figure 12: Influence of the width and height of the shallow banks near the channel wall on the leading upstream wave amplitude.

and $h_2 = 0.6$. In figures 11(b) and 11(d) the depth h_2 is changed to 0.5 and 0.8, respectively, while maintaining the same values for W_1, W_2 and W_3 as in figure 11(a). In figure 11(c) the widths are $W = (1, 2, 7)$, and in figure 11(e) the widths are $W = (6, 2, 2)$, and the depths h_1 and h_2 are the same as in figure 11(a).

The variation in the wave pattern displayed in these results clearly depend both on the width mean Froude number

$$\overline{F} = \frac{1}{W} \int_0^W F(y)\, dy \,,$$

and on the channel configuration. Table 1 shows the width mean Froude number and the width mean wave amplitude of the leading upstream wave for the five plots in figure 11. Although the increase in wave amplitude near

	(a)	(b)	(c)	(d)	(e)
$\overline{F}$	0.9368	0.9932	0.9833	0.8561	0.8669
$\overline{\eta_{max}}$	0.0400	0.0648	0.1002	0.0170	0.0136

Table 1: Width-mean Froude number

critical $\overline{F}$ resemble the results from similar tests for channels with rectangular cross-channel profiles, the magnitude of the wave amplitude and the wave period is influenced by the depth variation, as seen in figures 11(b) and 11(c). The influence of the channel configuration is seen more clearly in figure 12, where the amplitude of the leading upstream wave is plotted as a function of the width mean Froude number. These results suggest that at a given value of $\overline{F}$, the largest upstream waves will be generated in the channel whith the most narrow trench.

3.5 Effect of an initial acceleration

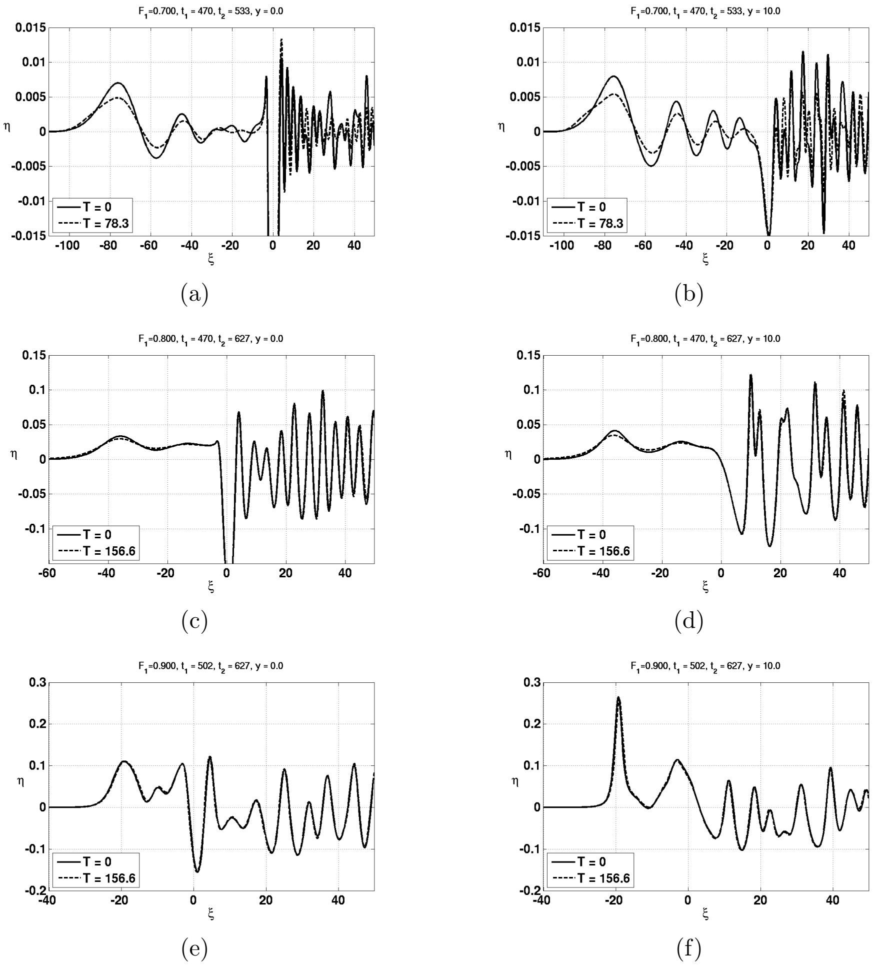

Figure 13: Comparison between results with and without acceleration from rest at the start of the simulation.

Jiang et al. discuss the sensitivity of the results to the starting condition, and conclude that different initial accelerations yield different results. In our simulations the pressure disturbance accelerates from rest to the designated speed over a single time step. In figure 13 we compare results for the abruptly started pressure propagation with results where the pressure disturbance accelerates from rest over a time T. Results are shown for a later time in the acceleration case than in the abrupt start case, to compensate for the delay in the generation of upstream waves in the former case.

Differences between the results are clearly visible for $F_1 = 0.7$, where the upstream wave generation is transient in nature. A slight deviation is also visible in the upstream waves for $F_1 = 0.8$, but the deviations clearly diminish with increasing F_1. We therefore conclude that the deviations due to the starting condition mainly influences the transient wave phenomena, and to lesser extent the wave pattern attained after long times.

4 Concluding remarks

In section 3 we have presented results for wave generation and propagation in a channel with a variable cross-channel topography. A case study for a similar channel configuration have previously been presented by Jiang et al.[2] for $F_1 = 1.0$. In figure 3(c) in Jiang et al. we clearly see a wave propagating upstream of the wave-generating disturbance. Our result for $F_1 = 1.0$ and $p_a = 0.1$, seen in figure 3(d), does not indicate upstream wave propagation. We do however find waves propagating upstream of the pressure disturbance if we increase the value of p_a, as seen in figure 14.

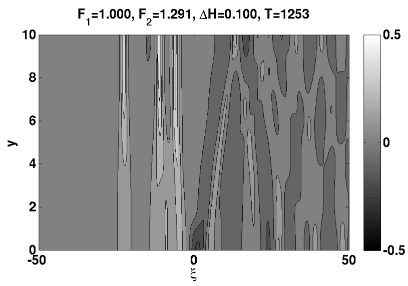

(a)

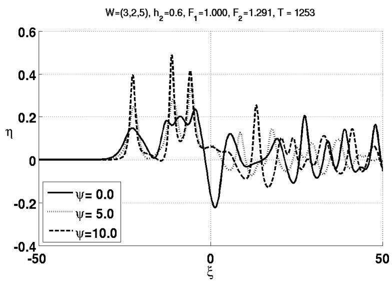

(b)

Figure 14: Wave pattern generated for $p_a = 0.15$

A word of caution is in order here. The Boussinesq equations tend to allow waves of unreasonably large amplitudes and wave speeds, when in reality instabilities will cause these waves to undergo wave breaking. The upstream wave in figure 14 propagates at a speed of $c_w/\sqrt{h_2} = 1.32$ relative to the local shallow water wave speed near the channel wall, which exceeds the largest possible wave speed for the solitary wave solution, given by Miles[11] as $c_w/c_0 = 1.294$. It is therefore questionable if the simulated result corresponds to a physically reasonable solution.

In this paper we have studied the wave generation and propagation in a channel with a variable cross-channel topography. We have found that waves may propagate upstream of the wave generating disturbance, and that the crest of these waves will span across the channel in a nearly straight line despite the variation in depth across the channel. The wave amplitude and generation time varies with the width-averaged Froude number $\overline{F}$, but is not governed by this parameter alone, as different configurations of widths and depths may result in different wave patterns for the same value of $\overline{F}$. We have also found that wave amplification may occur due to wave-wave interaction in the downstream wave packet,and can be maintained over long times. Although the variation in cross-channel topography seems to facilitate wave amplification, this does not seem to be a necessary condition for the occurrence of this phenomenon.

Acknowledgements

This work has received support from the Research Council of Norway through a grant to the program "Modelling of currents and waves for sea structures". We are indepted to Patrick Lynett for providing us with the latest version of the COULWAVE model, and to Philip L.-F. Liu and Tso-Ren Wu for guidance on how to use the model.

Appendix

In the TW model, the along channel wave propagation is computed by using a width averaged long wave model, such as the channel-Boussinesq model

$$2b\frac{\partial\tilde{\zeta}}{\partial t} + \frac{\partial}{\partial x}\left[2b(\tilde{h}+\tilde{\zeta})\bar{u}\right] = 0\,,$$

$$\frac{\partial\bar{u}}{\partial t} + \bar{u}\frac{\partial\bar{u}}{\partial x} + \frac{\partial\tilde{\zeta}}{\partial x} - \frac{1}{3}\kappa^2\tilde{h}^2\frac{\partial^3\bar{u}}{\partial x^2\partial t} = -\frac{\partial\tilde{p}_a}{\partial x}\,,$$

or the channel-KdV model

$$\frac{1}{c_0}\frac{\partial\tilde{\zeta}}{\partial t}+\left(1+\frac{3\tilde{\zeta}}{2\tilde{h}}\right)\frac{\partial\tilde{\zeta}}{\partial x}+\frac{1}{6}\kappa^2\tilde{h}^2\frac{\partial^3\tilde{\zeta}}{\partial x^3}+\left(\frac{1}{4\tilde{h}}\frac{\partial\tilde{h}}{\partial x}+\frac{1}{2b}\frac{\partial b}{\partial x}\right)=-\frac{1}{2}\frac{\partial\tilde{p}_a}{\partial x},$$

where $c_0=(g\tilde{h})^{\frac{1}{2}}$ is a chracteristic speed, and the *shape factor* κ^2 is determined by the channel geometry (see e.g. Teng and Wu[17, 18, 19]). Width averages and cross section averages are computed by

$$\tilde{(\cdot)}=\frac{1}{2b}\int_{-b}^{b}(\cdot)\,dy\,,$$

$$\bar{(\cdot)}=\frac{1}{A_0}\iint_{A_0}(\cdot)\,dy\,dz\,,$$

where $2b$ is the channel width at $z=0$ and A_0 is the equilibrium area of the cross section. The general formulation allows b to vary in the along-channel direction, but we have only used a constan value for b in our applications. The cross channel perturbation is found by solving the Poisson equation with boundary conditions

$$\begin{aligned}\Psi_{yy}+\Psi_{zz}&=1\,,\\ \Psi_z|_{z=0}&=\tilde{h}\,,\quad\text{(at the frees surface)}\,,\\ \Psi_n&=0\,,\quad\text{(at channel walls below the}\\ &\qquad\qquad\text{unperturbed water surface)}\,,\end{aligned}$$

where n is the unit normal vector at the solid boundaries. This determines the shape factor

$$\kappa^2=\frac{3}{\tilde{h}}(\tilde{\Psi}-\bar{\Psi})\,.$$

The width averaged solitary wave solution with amplitude α is

$$\tilde{\zeta}=\alpha\,\mathrm{sech}^2\sqrt{\frac{3\alpha}{4\kappa^2}}(x-ct)\,,$$

and the width averaged solution to the linearized problem can be written in terms of the Airy function Ai as

$$\tilde{\zeta}=\beta\left(\tfrac{1}{2}\kappa^2\tilde{h}^2t\right)^{-\frac{1}{3}}Ai\left[-x\left(\tfrac{1}{2}\kappa^2\tilde{h}^2t\right)^{-\frac{1}{3}}\right],$$

where β determines the wave amplitude. The wave profile including cross channel effects is

$$\zeta(x,y,t)=\tilde{\zeta}(x,t)-(\Psi|_{z=0}-\tilde{\Psi})\tilde{\zeta}_{xx}$$

The problem outlined above has been solved using the Poisson solver included in MATLAB.

References

[1] R. C. Ertekin, W. C. Webster, and J. V. Wehausen. Waves caused by a moving disturbance in a shallow channel of finite width. *J. Fluid Mech.*, 169:275–292, 1986.

[2] T. Jiang, R. Henn, and S. D. Sharma. Wash waves generated by ships moving on fairways of varying topography. In *Proceedings for the 24th Symposium on Naval Hydrodynamics*, Fukuoka, 2002.

[3] C. Katsis and T. R. Akylas. On the exitation of long nonlinear water waves by a moving pressure distribution. part 2. three-dimensional effects. *J. Fluid Mech.*, 177:49–65, 1987.

[4] P. L.-F. Liu. Model equations for wave propagation from deep to shallow water. *Adv. Coastal Engng.*, 1:125–157, 1994.

[5] P. L.-F. Liu and T.-R. Wu. Waves generated by moving pressure disturbances in rectangular and trapezoidal channels. *Journal of Hydraulic Research*, 42(2):163–171, 2004.

[6] P. Lynett and P. L.-F. Liu. Coulwave model page: Modeling wave generation, evolution, and interaction with depth-integrated, dispersive wave equations. http://ceprofs.tamu.edu/plynett/COULWAVE/.

[7] P. Lynett and P. L.-F. Liu. A numerical study of submarine landslide generated waves and runup. *Royal Society of London A*, 458(2028):2885–2910, 2002.

[8] P. Lynett, T.-R. Wu, and P. L.-F. Liu. Modeling wave runup with depth-integrated equations. *Coast. Engrg.*, 46(2):89–107, 2002.

[9] P. A. Madsen and H. A. Schäffer. Higher-order boussinesq-type equations for surface gravity waves: Derivation and analysis. *Phil. Trans. R. Soc. Lond. A*, 356:3123–3184, 1998.

[10] J. Mathew and T. R. Akylas. On three-dimensional long water waves in a channel with sloping sidewalls. *J. Fluid Mech.*, 215:289–307, 1990.

[11] J. W. Miles. Solitary waves. *Ann. Rev. Fluid Mech.*, 12:11–43, 1980.

[12] O. Nwogu. Alternative form of boussinesq equations for nearshore wave propagation. *Journal of waterway, port, coastal, and ocean engineering*, 119(6):618–638, 1993.

[13] G. Pedersen. Three-dimensional wave patterns generated by moving disturbances at transcritical speeds. *J. Fluid Mech.*, 196:39–63, 1988.

[14] D. H. Peregrine. Long waves in a uniform channel of arbitrary cross-section. *J. Fluid Mech.*, 32(2):353–365, 1968.

[15] A. S. Peters. Rotational and irrotational solitary waves in a channel with arbitrary cross-section. *Commun. pure appl. Math*, 19:445–471, 1966.

[16] P Peterson, T Soomere, J Engelbrecht, and E. van Groesen. Soliton interaction as a possible model for extreme waves in shallow water. *Nonlinear Processes in Geophysics*, 10:503–510, 2003.

[17] M. H. Teng and T. Y. Wu. Nonlinear water waves in channels of arbitreary shape. *J. Fluid Mech.*, 242:211–233, 1992.

[18] M. H. Teng and T. Y. Wu. Evolution of long water waves in variable channels. *J. Fluid Mech.*, 266:303–317, 1994.

[19] M. H. Teng and T. Y. Wu. Effects of channel cross-sectional geometry on long wave generation and propagation. *Phys. Fluids*, 9(11):3368–3377, 1997.

[20] G. Wei, J. T. Kirby, S. T. Grilli, and R. Subramanya. A fully nonlinear boussinesq model for surface waves. part 1. highly nonlinear unsteady waves. *Journal of Fluid Mechanics*, 294:71–92, 1995.